Photos: Corbis, DOI: 10.2516/ogst/2012104, IFPEN, X.

Dossier

This paper is a part of the hereunder thematic dossier published in OGST Journal, Vol. 68, No. 6, pp. 951-1113 and available online here

Cet article fait partie du dossier thématique ci-dessous publié dans la revue OGST, Vol. 68, n°6, pp. 951-1113 et téléchargeable ici

DOSSIER Edited by/Sous la direction de : **C. Barrère-Tricca**

IFP Energies nouvelles International Conference / Les Rencontres Scientifiques d'IFP Energies nouvelles

MAPI 2012: Multiscale Approaches for Process Innovation

MAPI 2012 : Approches multi-échelles pour l'innovation des procédés

Oil & Gas Science and Technology – Rev. IFP Energies nouvelles, Vol. 68 (2013), No. 6, pp. 951-1113

Oil & Gas Science and Technology – Rev. IFP Energies nouvelles, Vol. 68 (2013), No. 6, pp. 1007-1026

DOI: 10.2516/ogst/2012069

IFP Energies nouvelles International Conference
Rencontres Scientifiques d'IFP Energies nouvelles

MAPI 2012: Multiscale Approaches for Process Innovation
MAPI 2012 : Approches multi-échelles pour l'innovation des procédés

From Detailed Description of Chemical Reacting Carbon Particles to Subgrid Models for CFD

S. Schulze, M. Kestel, P.A. Nikrityuk* and D. Safronov

CIC Virtuhcon, Department of Energy Process Engineering and Chemical Engineering, Technische Universität Bergakademie Freiberg, 09599 Freiberg - Germany
e-mail: Sebastian.Schulze@vtc.tu-freiberg.de - Matthias.Kestel@vtc.tu-freiberg.de - Petr.Nikrityuk@vtc.tu-freiberg.de - Dmitry.Safronov@vtc.tu-freiberg.de

* Corresponding author

Résumé — De la description détaillée des particules de carbone chimiquement réactives aux modèles de sous-maille pour la CFD — Cette étude est consacrée au développement et à la validation d'un sous-modèle pour l'oxydation partielle d'une particule de charbon sphérique se déplaçant dans une atmosphère air/vapeur. Le diamètre de la particule est de 2 mm. La particule de charbon est représentée par du carbone non poreux exempt d'humidité et de cendres, alors que la qualité du charbon est établie en utilisant des expressions du taux de réaction semi-globale extraites de la littérature. Le sous-modèle inclut six espèces chimiques gazeuses (O_2, CO_2, CO, H_2O, H_2, N_2). Trois réactions hétérogènes sont utilisées, ainsi que deux réactions semi-globales homogènes, à savoir l'oxydation du monoxyde de carbone et la réaction du gaz à l'eau. Les particularités distinctives du modèle de sous-maille se trouvent dans la prise en compte de l'influence des réactions homogènes sur les caractéristiques intégrales telles que les taux de combustion du carbone et la température de la particule. Le sous-modèle a été validé en comparant ses résultats avec un modèle complet basé sur la CFD résolvant les questions de flux volumique et de couche limite autour de la particule. Dans ce modèle, les équations de Navier-Stokes couplées aux équations de conservation de l'énergie et des espèces ont été utilisées pour résoudre le problème au moyen de l'approche en état pseudo-stationnaire. À la surface de la particule, l'équilibre de la masse, de l'énergie et de la concentration des espèces a été appliqué, y compris l'effet de l'écoulement de Stefan et l'effet de la perte de chaleur due aux rayonnements à la surface de la particule. Une bonne adéquation a été atteinte entre le sous-modèle et le modèle basé sur la CFD. En outre, le modèle basé sur la CFD a été comparé aux données expérimentales publiées dans la littérature (Makino *et al.* (2003) *Combust. Flame* 132, 743-753). Une bonne concordance a été atteinte entre les données prédites numériquement et celles obtenues expérimentalement pour les conditions d'entrée correspondant au régime contrôlé par la cinétique. La divergence maximale (10 %) entre les expériences et les résultats numériques a été observée dans le régime contrôlé par la diffusion. Enfin, nous discutons de l'influence du nombre de Reynolds, de la fraction massique d'O_2 ambiant et de la température ambiante sur le comportement de la particule de charbon.

Abstract — From Detailed Description of Chemical Reacting Carbon Particles to Subgrid Models for CFD — *This work is devoted to the development and validation of a sub-model for the partial oxidation of a spherical char particle moving in an air/steam atmosphere. The particle diameter is 2 mm. The coal particle is represented by moisture- and ash-free nonporous carbon while the coal rank is implemented using semi-global reaction rate expressions taken from the literature. The submodel includes six gaseous chemical species (O_2, CO_2, CO, H_2O, H_2, N_2). Three heterogeneous reactions are employed, along with two homogeneous semi-global reactions, namely carbon monoxide oxidation and*

the water-gas-shift reaction. The distinguishing feature of the subgrid model is that it takes into account the influence of homogeneous reactions on integral characteristics such as carbon combustion rates and particle temperature. The sub-model was validated by comparing its results with a comprehensive CFD-based model resolving the issues of bulk flow and boundary layer around the particle. In this model, the Navier-Stokes equations coupled with the energy and species conservation equations were used to solve the problem by means of the pseudo-steady state approach. At the surface of the particle, the balance of mass, energy and species concentration was applied including the effect of the Stefan flow and heat loss due to radiation at the surface of the particle. Good agreement was achieved between the sub-model and the CFD-based model. Additionally, the CFD-based model was verified against experimental data published in the literature (Makino et al. *(2003)* Combust. Flame *132, 743-753). Good agreement was achieved between numerically predicted and experimentally obtained data for input conditions corresponding to the kinetically controlled regime. The maximal discrepancy (10%) between the experiments and the numerical results was observed in the diffusion-controlled regime. Finally, we discuss the influence of the Reynolds number, the ambient O_2 mass fraction and the ambient temperature on the char particle behaviour.*

INTRODUCTION

Nowadays, due to the continuous increase in CO_2 emissions around the world, traditional power generation using coal as a primary fuel can be considered a waste of carbon. Coal is and will continue to be basically considered as a primary chemical feedstock for the production of gasoline, fertilizers or other chemicals using so-called "coal gasification". For a review of gasification technology development, we refer to the book [2]. Along with coal gasification one other possible way to reduce CO_2 emissions is to use the so-called "oxy-combustion" of coal with flue gas recirculation and carbon sequestration. For a review of technological development, we refer to the works [3, 4].

In the design of novel combustors or gasifiers working on solid carbonaceous fuels (particles), the important issue is the adequate prediction of the basic characteristics of such devices. Due to the complexity of physical and chemical processes inside gasifiers or combustors, experimental studies are not always capable of characterizing the basic features of all related phenomena. Therefore, computer simulation models such as Euler-Euler or Euler-Lagrange models have become well-established tools for understanding and optimizing fluid-particle flows in combustors and gasifiers. It should be noted that all these models use Computational Fluid Dynamics (CFD) equations and algorithms. For instance, a number of works have been published recently on the numerical modeling of pilot-scale gasifiers, *e.g.* [5–9], and oxy-fuel combustors, *e.g.* the review [10]. An analysis of these works shows that the distinguishing feature of all CFD-based simulations of combustors and gasifiers is the use of so-called computational sub-models describing particle-gas interactions on the microscale level, *e.g.* the burning rate of a particle and the particle temperature.

It should be noted that in spite of significant progress in the development of macroscale models for particulate flows and their numerical implementation in many commercial codes (ANSYS-Fluent, -CFX, *e.g.* see the work [11]), and open-source codes (openFOAM, *e.g.* see the work [12]), the sub-models which are used in the macroscale simulations, correspond to the models developed in the early 1970s, see the works [13, 14]. One of the first subgrid models introduced by Baum and Street [13] and Smith [14] were based on the so-called "circuit analog" where kinetically controlled and diffusion-controlled reaction rates represent fictitious electric resistance placed sequentially in one electrical circuit. This class of models, which is sometimes called a kinetic/diffusion rate model, is based on the assumption that the heterogeneous reactions occur at the particle surface. Until now the well-known Baum and Street model, which is used for example as a default submodel in the commercial CFD-software Fluent, has referred to so-called "surface reaction models". These models were developed and are still used for modeling coal particle combustion taking into account the basic carbon-oxygen reaction, $C + O_2$. Furthermore, the mass fractions of gaseous species at the particle surface are not taken into account in this model and gasification reactions are largely not considered. Moreover, the influence of particle velocity on the particle combustion rate is not well introduced. It should be noted that one of the first submodels for a moving chemically reacting char particle was developed by Tu *et al.* [15], Parker and Hottel [16], who took into the acount the Reynolds number in their mathematical description of the burning rates of char particles. However, these findings were not directly utilized in kinetic/diffusion-based submodels.

Until now, however, in spite of their many disadvantages, kinetic/diffusion-based models tuned using additional coefficients have showed surprisingly good performances during numerical simulations of pulverized coal gasification in entrained-flow gasifiers in respect to thier agreement with experimental data, *e.g.* see the works [8] and [9, 17], where the commercial software Fluent6.3. and ANSYS-Fluent12 were utilized, respectively. In the case of work [17], the

kinetic/diffusion rate model was modified using an additional term characterising a moving flame front. In work [9], where a kinetic/diffusion model was used, the values of the pre-exponential factor and the activation energy for some chemical reactions were "modified slightly in accordance with the comparison between numerical simulations and experimental data" (citation).

Sijercic and Hanjalic [6] adopted the kinetic/diffusion rate model for modelling pulverized coal gasification taking into account the so-called gasification reactions $C + CO_2$ and $C + H_2O$ and the influence of particle velocity on the oxidation rate of a char particle. However, the surface concentrations of O_2, CO_2 and H_2O were eliminated from their considerations when calculating carbon consumption rates. An advanced sub-model was developed by Hayhurst [18], who reconsidered simple models for the burning of a porous coal char particle taking into account the influence of convection on the interfacial mass transfer in one-film and two-film model approaches. However, the model was not validated against experimental or CFD-based numerical simulations. For recent reviews of the common char oxidation sub-models, we refer to the works [10, 19]. According to these reviews, the correct prediction of the particle burning rate and the particle temperature is an essential part of successfully modelling gasifiers/combustors. Finally, it should be emphasized that the development of accurate submodels for chemically reacting char particles depends on the understanding of interfacial phenomena occurring near and on the particle surface. This understanding can be achieved by carrying out experiments and detailed numerical simulations, which have to be validated against experiments.

Recently, parallel to the advanced experimental studies of char particle combustion, *e.g.* see [20, 21], CFD-based particle-resolved numerical modelling of such processes has become a standard tool for understanding and predicting coal particle behavior in a hot gaseous environment. In particular, with significant progress in computational methods and computational hardware, a rapid increase can be detected in publications devoted to CFD-based numerical simulations a chemically reacting coal particles, *e.g.* see [22–26]. For instance, Lee *et al.* [26] carried out one-dimensional fully transient numerical simulations of the chemically reacting flow field on and around the surface of an isolated carbon particle. Computations were performed for a spherically symmetric system. It was shown that for small particles (< 200 μm) transient gasification rates can deviate greatly from those predicted under the Pseudo-Steady-State approach (PSS). However, it should be noted that the authors used the so-called isobaric flow assumption, where the convection effect was represented by the Stefan flow only.

More advanced studies about the influence of convection on the oxidation of carbon particles have been performed recently. In particular, Blake [22] presented numerical simulations for the steady combustion of a spherical carbon particle in the slow viscous flow of an oxidizing ambient. In contrast to a work by Lee *et al*. [26], Blake [22] coupled the ambient convection, characterized by a small Reynolds number, with a strong radial convection, associated with the Stefan flow due to the particle mass loss. He found out, that in general, ambient convection increases the particle mass loss rate but has no effect in the kinetic control limit. The next significant contribution to the understanding of char particle behavior in a mixed convective environment came from Higuera [23]. In particular, he carried out a comprehensive CFD-based numerical study (in the framework of a steady-state approach coupled with a simple chemistry) on the influences of the size and velocity of the coal char particle, the temperature and the gas composition on the burning rate, the particle temperature and the extinction of the flame. It was shown that the Reynolds number of the particle plays a significant role in establishing the combustion or gasification regimes. However, no systematic analysis was carried out of the influence of the inflow temperature on the behavior of the particle with a fixed Reynolds number. Furthermore, there was no information in the paper about the grid resolution and the size of the computational domain and no code validation.

In conclusion, it should be noted that recent publications devoted to the CFD-based modelling of chemically reactive coal char particles moving in a hot oxidizing atmosphere (see the works [24, 25, 27]), basically describe the influence of input parameters such as the particle velocity, ambient temperature or particle diameter for single cases. However, no efforts have been made to transfer new knowledge gained in these new works to existing or novel surface reaction-based submodels. Motivated by this fact, in this work, we develop a sub-model for the partial oxidation of a spherical nonporous char particle moving in an air/steam atmosphere. The model is validated against a comprehensive CFD-based model, where the Navier-Stokes equations coupled with the energy and species conservation equations were used to solve the problem by means of the pseudo-steady state approach. Only the oxidation of the residual carbon, or coke, is considered. Following pioneering experiments by Gudmundsen and Smith [28] the time required to burn the fixed carbon is approximately 90 per cent of the total burning time for the coal particles. From this point of view, the char combustion/gasification sub-model is of great importance in the successful modeling of large-scale combustors or gasifiers.

1 PROBLEM FORMULATION

Before we proceed with the formulation of a sub-model, we next describe the computational setup used for CFD-based simulations. In particular, we consider a single spherical coal char particle with a diameter of $D = 2$ mm placed in

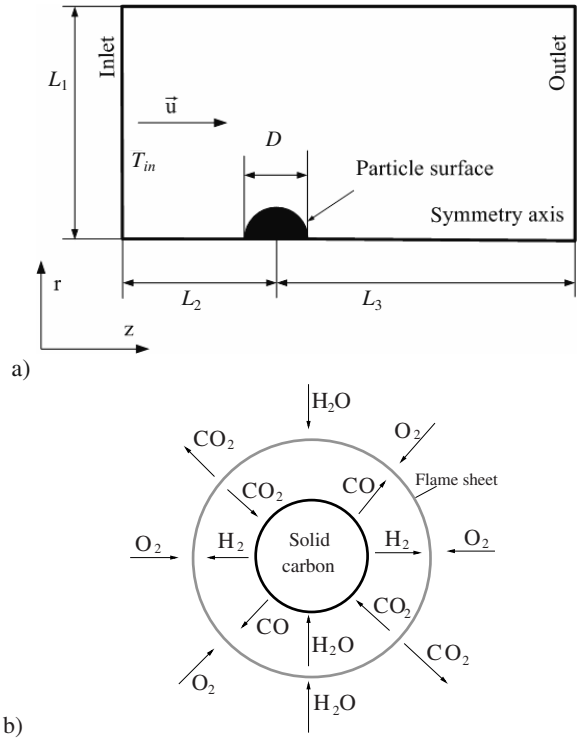

Figure 1

a) Principal scheme of the computational domain in cylindrical coordinates, b) schematic representation of char oxidation in the presence of water vapor.

a stationary position in a hot oxidizing environment with the main gas flow passing around it. The inflow velocity is assumed to be uniform and is determined by means of the Reynolds number calculated as:

$$Re = \frac{\rho_\infty u_\infty D}{\mu_\infty} \tag{1}$$

where ρ_∞ and μ_∞ are the density and molecular viscosity, respectively, corresponding to the inflow temperature T_{in} and the gas composition. Four Reynolds numbers are considered: 0, 10, 50 and 100, corresponding to the laminar flow regime.

Two cases with different inflow gas compositions are considered: the first case corresponds to the so-called dry air atmosphere with 0.233 mass fraction (Y) of O_2, 0.001 mass fraction of H_2O and with the rest of N_2, while the second case refers to the so-called reduced oxidation condition with $Y_{O_2} = 0.11$, $Y_{H_2O} = 0.074$ and $Y_{N_2} = 1 - Y_{H_2O} - Y_{O_2}$. For the fixed composition of the inflow gas, the inflow gas temperature T_{in} was varied from 1 000 K to 3 000 K. All calculations were accomplished at a total pressure of 1 bar. The modelling configuration and the size of the domain are illustrated in Figure 1 and Table 1. It can be seen that the ambient gas phase consists of O_2, CO_2, CO, H_2O, H_2 and N_2.

TABLE 1

Domain size and grid resolution

Case	L_1	L_2	L_3	Nodes
$Re = 0$	$75D$	$75D$	$75D$	23 205
$Re > 0$	$40D$	$30D$	$100D$	59 668

The chemistry is modelled using semi-global homogeneous and heterogeneous reactions written as follows [29]:

Heterogeneous (surface) reactions:

$$C + \frac{1}{2}O_2 \rightarrow CO \quad h^0_{R1} = -9.2 \text{ MJ kg}^{-1}\text{C} \tag{R1}$$

$$C + CO_2 \rightarrow 2CO \quad h^0_{R2} = 14.4 \text{ MJ kg}^{-1}\text{C} \tag{R2}$$

$$C + H_2O \rightarrow CO + H_2 \quad h^0_{R3} = 10.9 \text{ MJ kg}^{-1}\text{C} \tag{R3}$$

Homogeneous (gas phase) reactions:

$$CO + \frac{1}{2}O_2 \rightarrow CO_2 \quad h^0_{R4} = -10.1 \text{ MJ kg}^{-1}\text{CO} \tag{R4}$$

$$CO + H_2O \rightarrow CO_2 + H_2 \quad h^0_{R5} = -3.4 \text{ MJ kg}^{-1}\text{CO} \tag{R5}$$

$$CO_2 + H_2 \rightarrow CO + H_2O \quad h^0_{R6} = 3.4 \text{ MJ kg}^{-1}\text{CO} \tag{R6}$$

In reaction 5, steam H_2O plays the role of a catalyst [29, 30]. It should be noted that semi-global heterogeneous and homogeneous chemical reactions are widely used to model industrial combustors or gasifiers using computational fluid dynamics software, *e.g.* see [31]. However, at the same time it is a well-known fact that global reaction rates are often only valid in a certain range of conditions and should be used very cautiously, see [32, 33].

Finally, it should be noticed that the H_2-oxidation reaction ($H_2 + O_2$) was not taken into account in this work. For the dry air atmosphere, it is an acceptable assumption because under low steam concentration ($Y_{H_2O} = 0.001$) the water-gas-shift reaction does not play any important role in the balance of species. For the reduced oxidation condition ($Y_{H_2O} = 0.074$) at higher ambient temperatures the oxygen concentration near the carbon particle (within flame radius) is zero, thus H_2 (which is produced the reactions 3 and 5 on the particle surface and near the particle surface, respectively) does not react with O_2. However, at lower temperatures, when the oxygen concentration near the particle is not zero, an H_2- oxidation reaction can occur, thought the rate of reactions 3 and 5 at lower temperatures are low. In particular, estimated simulations carried out for the reduced oxidation condition at $T_{in} = 1\,200$ K showed that the discrepancy in $\dot{m}_C$ and T_s predicted with and without H_2-oxidation reaction does not exceed 4% or 3%, respectively.

2 CFD-BASED MODEL

To proceed with the description of the mathematical CFD-based model, several assumptions are introduced in order to solve the problem. In this work, we utilize the PSS approach, see [34], due to the fact that the consumption time of the particle is always large compared to the convective and diffusion time scales for the gas phase. The gas flow is treated as an incompressible ideal gas following the model described in [35].

Before we proceed with the mathematical formulation of a model, several assumptions are introduced:

– the particle shape is spherical and the gas flow is symmetrical;
– the porosity of the particle is not taken into account, thus the intraparticle diffusion is neglected. The surface reaction model is used to simulate the interaction between the reacting solid surface and the gas phase;
– the particle consists of carbon only. In particular, the drying and devolatilization of the particle is not included due to the steady-state character of the model;
– the radiation of the gas phase is not taken into account. It should be noted that this assumption is a rough approximation, which can lead to the overestimation of the particle-surface temperature;
– the buoyancy effect is neglected.

Before we proceed with the formulation of the mathematical models, we would like to discuss some limitations, which follow from the assumptions used in this work. First, our basic assumption is that heterogeneous reactions occur on the particle surface only. Thus, the carbon consumption is only correlated to the outer surface of the particle. However, it is a well-known fact that partial oxidation of a char particle at lower ambient temperatures $T_{in} < 1\,000$ K (in a gasification regime) occurs inside the particle, namely in pores. To overcome this limitation a random pore model [36] can be applied. Accordingly, in this case the so-called intrinsic kinetics for all heterogeneous reaction are required. So far, however, there has been little discussions in the literature about CFD-based models describing char conversion under the influence of an ambient gas flow where intrinsic kinetic used. Basic models, *e.g.* the so-called shrinking reacted core model, consider only the diffusion-controlled oxidation of char [37, 38] taking into account intraparticle diffusion and intrinsic reactivity under isothermal conditions. The next problem is that interplay between porosity and the gas flow should be taken into account. Recently, Witting *et al.* [39] showed numerically that in some cases the gas flow can penetrate the porous particle at moderate *Re* numbers and high porosity values. With this in mind, as a first step we assume that the heterogeneous reactions occur only on the particle surface.

In conclusion, the neglecting of drying and devolatilization is explained by the fact that subgrid models for coal conversion are basically split on three submodels, namely, drying, devolatilization and char conversion [8, 17]. In order to validate a sub-model for the partial oxidation of a spherical nonporous char particle moving in an air/steam atmosphere, we use a comprehensive CFD-based model where the oxidation of the residual carbon, or coke, is considered.

Taking into account these assumptions, the complete set of governing equations takes the following form:

$$\nabla \cdot (\rho\, \vec{u}) = 0 \tag{2}$$

$$\nabla \cdot (\rho\, \vec{u} \otimes \vec{u}) = -\nabla p + \nabla \cdot (\bar{\bar{\tau}}) \tag{3}$$

$$\nabla \cdot (\rho\, \vec{u}\, Y_i) = \nabla \cdot (\rho\, D_i\, \nabla Y_i) + R_i \tag{4}$$

$$\nabla \cdot (\rho\, \vec{u}\, h) = \nabla \cdot (\lambda \nabla T) - \sum_{r}^{N_R} h^0_{r,j} R_{r,j} \tag{5}$$

$$\rho = \frac{p}{R\,T\,\sum_i \frac{Y_i}{M_i}} \tag{6}$$

where $\bar{\bar{\tau}} = \mu[(\nabla \vec{u} + \nabla \vec{u}^T)]$ is the stress tensor and i stands for the participating reactants O_2, CO_2, CO, H_2 and H_2O. The mass fraction for N_2 is calculated as $Y_{N_2} = 1 - \sum_i Y_i$. In Equation (3), $\otimes$ denotes the dyadic product of two vectors.

Equation (7) depicts the species net production rate R_i, where i stands for the ith species and r for the rth reaction. It is computed as the sum of the Arrhenius reaction sources over the N_R reactions in which the species are involved:

$$R_i = M_i \sum_r \widehat{R}_{i,r} \tag{7}$$

Here, the Arrhenius molar rate of creation/destruction $\widehat{R}_{i,r}$ is calculated as:

$$\widehat{R}_{i,r} = \left(\nu''_{i,r} - \nu'_{i,r}\right) \left(k_r \prod_{j=1}^{N} \left[C_{j,r}\right]^{\left(\eta'_{j,r} - \eta''_{j,r}\right)} \right) \tag{8}$$

for a homogeneous reaction, where $\nu'_{i,r}$ is the stoichiometric coefficient for reactant i in reaction r and $\nu''_{i,r}$ is the stoichiometric coefficient for product i in reaction r. $\eta'_{j,r}$ and $\eta''_{j,r}$ are the forward and backward rate exponents for each reactant and product species j in reaction r, respectively.

2.1 Boundary Conditions

At the surface of the particle, the balance of mass, energy and species concentration is applied including the effect of the Stefan flow and the heat loss due to radiation at the particle surface. Due to the fact that heterogeneous reactions affect the mass and energy balance at the interface, they have an important influence on the boundary conditions for the gas species and the temperature. The convective and diffusive mass fluxes of the gas-phase species at the surface are

TABLE 2

Kinetic coefficients for chemical reactions

Reaction No.	A_r	n_T	E_A	Ref.
1	3.007×10^5 m s^{-1}	0	1.4937×10^5 J.mol^{-1}	[41]
2	4.605 m s^{-1}K^{-1}	1	1.751×10^5 J.mol^{-1}	[42]
3	11.25 m s^{-1}K^{-1}	1	1.751×10^5 J.mol^{-1}	[42]
4	2.24×10^{12} m$^{2.25}$ kmol$^{-0.75}$s^{-1}	0	1.6736×10^5 J.mol^{-1}	[29, 30]
5	2.74×10^9 m^3 kmol^{-1}s^{-1}	0	8.368×10^4 J.mol^{-1}	[43]
6	1.00×10^8 m^3 mol^{-1}s^{-1}	0	1.205×10^5 J.mol^{-1}	–

balanced by the production/destruction rates of gas-phase species caused by surface reactions (see [40]):

$$\rho_S D_i \frac{\partial Y_{i,S}}{\partial n} - \dot{m}_C^{'} Y_{i,S} = M_i \widehat{R}_{i,s} \tag{9}$$

$$\dot{m}_C^{'} = \sum_{i=1}^{N_R} M_i \widehat{R}_{i,s} = \sum_{i=1}^{N_R} \dot{m}_{C,i}^{'} \tag{10}$$

$$\mathbf{n} \cdot \lambda \nabla T|_{gas} = \sum_{j=1}^{N_R} \dot{m}_{C,j}^{'} h_j^0 + \epsilon_S \sigma (T_{in}^4 - T_S^4) \tag{11}$$

where $\widehat{R}_{i,s}$ (kmol/m^2 s) is the production rate of species i due to the surface reaction, $\dot{m}_C^{'}$ is the net mass flux between the surface and the gas, the index $_{gas}$ refers to the gas side at the wall and $\mathbf{n}$ is the vector normal to the wall. Here ϵ_S is the particle emissivity, which conforms to the emissivity of a black body ($\epsilon_S = 1$). It should be noted that the heat flux into the solid in Equation (11) was neglected. This is an acceptable condition while $\lambda_s/\lambda_{gas} \gg 1$.

Basically, on a chemically nonreacting solid surface the fluid velocity on a solid wall is zero, which corresponds to the well-known no-slip boundary condition. However, if a heterogeneous chemical reaction occurs on the solid surface, then the velocity can be nonzero. This flow is called the Stefan flow and characterizes the net mass flux between the surface and the gas. Hence, the heterogeneous reaction-induced Stefan velocity takes the following form:

$$\mathbf{n} \cdot \vec{u} = \frac{\dot{m}_C^{'}}{\rho} \tag{12}$$

2.2 Reaction Kinetics and Transport Properties

The kinetic coefficients k_r of chemical reactions (2) through (7) are calculated using the extended Arrhenius expression:

$$k_r = A_r T_s^{n_T} \exp(E_A/(R T_s)) \tag{13}$$

where A_r is the pre-exponential factor, n_T is the temperature exponent and E_A is the activation energy. The values for A_r, n_T and E_A with corresponding units are given in Table 2 [29, 30, 41–43].

Notice that the CO oxidation-reaction order (reaction 4) is not directly related to the stoichiometric coefficient of the reaction due to the global character of this reaction. Finally, we note that the reaction $C + 2H_2$ was not included in considerations because its rate is much lower than those of the other heterogeneous reactions.

The heat capacity of the mixture was calculated as follows:

$$c_p = \sum_i Y_i c_{p,i}$$

$$c_{p,i} = A_i + B_i T + C_i T^2 + D_i T^3 + E_i T^4 \tag{14}$$

where $c_{p,i}$ is the specific heat capacity of the single species at constant pressure. The polynomial coefficients are taken from [44]. The values for λ, μ and D are calculated using kinetic theory. In particular, the dynamic viscosity for the single species μ_i is computed as follows:

$$\mu_i = 2.67 \cdot 10^{-6} \frac{\sqrt{M_{w,i} T}}{\sigma_i^2 \Omega_{\mu,i}}, \qquad \Omega_{\mu,i} = \Omega_{\mu,i}(T_i^*) \tag{15}$$

Here, $\Omega_{\mu,i}$ is the viscous collision integral with $T_i^* = \frac{T}{(\epsilon/k_B)_i}$.

The thermal conductivity for the particular species λ_i is defined as a function of μ_i and $c_{p,i}$:

$$\lambda_i = \frac{15}{4} \frac{R}{M_{w,i}} \mu_i \left[\frac{4}{15} \frac{c_{p,i} M_{w,i}}{R} + \frac{1}{3} \right] \tag{16}$$

For the calculation of μ and λ for the mixture, we use kinetic theory and the ideal gas law as follows:

$$\Phi = \sum_i \frac{\chi_i \Phi_i}{\sum_j \chi_j \psi_{ij}}, \quad \psi_{ij} = \frac{\left[1 + \left(\frac{\Phi_i}{\Phi_j} \right)^{1/2} \left(\frac{M_{w,j}}{M_{w,i}} \right)^{1/4} \right]^2}{\left[8 \left(1 + \frac{M_{w,j}}{M_{w,i}} \right) \right]^{1/2}} \tag{17}$$

Here, χ is the mole fraction, Φ corresponds to μ or λ.

The diffusion coefficient $D_{i,m}$ for the species i in the mixture m is computed taking into account the local mole fractions of the individual species of the mixture:

$$D_{i,m} = \frac{1 - X_i}{\sum_{j, j \neq i} (X_j / D_{i,j})} \tag{18}$$

$$D_{ij} = 0.0188 \frac{\left[T^3 \left(\frac{1}{M_{w,i}} + \frac{1}{M_{w,j}} \right) \right]^{\frac{1}{2}}}{p_{abs} \sigma_{ij}^2 \Omega_D}$$

Here, D_{ij} is the diffusion coefficient for a binary mixture, Ω_D is the diffusive collision integral, which describes the interaction between molecules and σ_{ij} is the average collision diameter for the binary mixture. The values for σ_i and ϵ/k_B were taken from [45] as default values.

3 SUB-MODEL

Due to the multiscale character of chemically reacting particulate flows in gasifiers/combustors, very often so-called zero-dimensional (0D) heat and mass transfer models are used to calculate the dynamics of carbon consumptions rates for each particle. In this class of models, basically, no transport equations in the form of Equations (4) and (5) are solved. In spite of that so-called semi-empirical relations are used to evaluate the phenomena occurring inside each cell of the grid, *e.g.* see the book [46]. In particular, to calculate the heat and mass transfer between coal particles and the bulk gas, so-called semi-empirical Nu-based relations are used. Next, we enhance the well-known 0-D heat transfer model to predict the char particle behaviour in a hot gaseous environment. The distinguishing feature of this subgrid model is that it takes into account the influence of homogeneous reactions on integral characteristics such as the carbon consumption rates and the particle temperature. In particular, to take into account the influence of homogeneous reactions on the carbon consumption rates, we introduce a virtual flamesheet, which has a volume V_F, near the particle where homogeneous reactions occur, see Figure 2. Next, we present a mathematical formulation of the submodel.

The subgrid energy-balance equation takes the following form:

$$m_p\, c_p\, \frac{dT_s}{dt} = A_p\, \alpha\, (T_\infty - T_s) + A_p\, \varepsilon_S\, \sigma \left(T_\infty^4 - T_s^4\right) - A_p \sum_r^{N_R} \dot{m}'_{\mathrm{C},r}\, h_r^0 - V_F \sum_r^{N_R} h_{r,j}^0\, R_{r,j} \tag{19}$$

The subgrid species balance equations:

$$\beta\, (c_{i,\infty} - c_{i,S}) = \widehat{R}_{i,s} + \frac{V_F}{A_P}\, \widehat{R}_i \tag{20}$$

where the particle surface, A_p, and the 'flame' volume, V_F, are calculated as follows:

$$A_P = 4\,\pi\, r_S^2 \qquad V_F = \frac{4}{3}\,\pi\, \left(r_F^3 - r_S^3\right) \tag{21}$$

Here, r_S describes the particle radius and r_F is the external flame radius.

The molar concentration c can be calculated depending on the mass fraction in the following way:

$$c_i = \frac{\tilde{M}}{M_i}\, \frac{p}{R\,T}\, Y_i = \frac{\rho}{M_i} Y_i \tag{22}$$

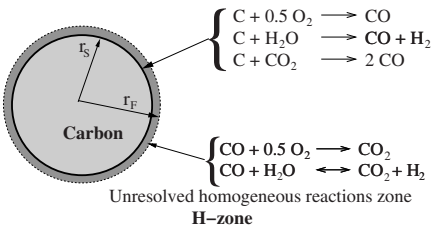

Figure 2

Principal scheme of reactions zones used in subgrid model.

Thus, Equation (20) can be written as follows:

$$\frac{\beta\, \rho_S}{M_i}\, (Y_{i,\infty} - Y_{i,S}) = \widehat{R}_{i,s} + \frac{V_F}{A_P}\, R_i \tag{23}$$

Here, β is the mass transport coefficient and, c_∞ and c_S are the species molar concentrations in the ambient atmosphere and at the particle surface, respectively. To simplify the model, we assumed that $\rho_S \approx \rho_\infty$.

The heat transfer coefficient α and the mass transfer coefficient β are calculated using the Nusselt and Sherwood numbers, respectively:

$$Nu = \frac{\alpha\, D}{\lambda_\infty}, \qquad Sh = \frac{\beta\, D}{D_{Le}} \tag{24}$$

where λ is the thermal conductivity and D_{Le} is the diffusion coefficient calculated from the following relation:

$$Le = \frac{\lambda_\infty}{D_{Le}\, c_{p\infty}\, \rho_\infty} = 1 \tag{25}$$

Here, we assumed that the Lewis number Le is equal to unity, which is a frequently used assumption for modeling coal combustion using one-film and two-film models, *e.g.* see [29].

The Prandtl number Pr and the Schmidt number Sc are derived as the following:

$$Pr = \frac{\nu_\infty}{a_\infty} = \frac{\mu_\infty\, c_{p\infty}}{\lambda_\infty}, \qquad Sc = \frac{\nu_\infty}{D_{Le}} \tag{26}$$

where ν is the kinematic viscosity, a is the thermal diffusivity and μ is the dynamic viscosity. Following the assumption that the Lewis number is unity, the Schmidt and Prandtl numbers are equal, leading to $Nu = Sh$.

The Nusselt number is calculated using modified Ranz and Marshall relation [47, 48]:

$$Nu = 1.7 + 0.664 Re^{\frac{1}{2}} Pr^{\frac{1}{3}} \tag{27}$$

where Re is calculated using Equation (1).

The comparison of equations representing boundary conditions (*see Eq. 9-11*) with Equations (19) and (23) reveal

similarity in some terms. The only difference is the introduction of a 'virtual flamesheet' consisting of homogeneous chemical reactions.

The carbon mass flow can be calculated using the surface area of the particle and interfacial species concentrations which are used in heterogeneous reactions:

$$\dot{m}_C = 4\pi r_S^2 \, \rho_S \, M_C \cdot \left(2\, k_{R1} \frac{Y_{O_2,S}}{M_{O_2}} + k_{R2} \frac{Y_{CO_2,S}}{M_{CO_2}} + k_{R3} \frac{Y_{H_2O,S}}{M_{H_2O}} \right) \tag{28}$$

It should be noted that in contrast to the basic subgrid model developed for the modelling of pulverized coal gasification/combustion (*e.g.* see [6, 13, 14]), in this model, we use interfacial values of the species mass fractions in stead of bulk values in Equation (28). However, this condition requires the whole system of balance equations to be solved iteratively. A detailed description of each balance equation is given in Appendix A. We note that the values of T_{in} used in the CFD-based model correspond to the values of $T_\infty = T_{in}$ utilized in the subgrid model.

4 NUMERICS AND VALIDATION

Commercial software [45] was adopted to solve the problem under consideration. In particular, the governing equations (2-5) were solved following an implicit finite-volume technique. For pressure-velocity coupling the SIMPLE algorithm was used [49]. The convective terms in all equations were discretized by means of the QUICK scheme [50]. The proper size of the domain and the grid resolution were chosen by calculating the drag coefficient C_D and comparing it with tabulated data published in the literature. Good agreement was observed between our simulations and published data. The details are published elsewhere [25] and not repeated here.

Finally, it should be noted that in order to resolve the flame sheet and the thermal and chemical species boundary layers properly we had to use grid refinement near the particle surface. In particular, Figure 3 shows the grids used in the simulations, including a zoomed view near the particle surface, where a and b are the nondimensional size of the control volumes near the particle surface scaled with the particle diameter D. In particular, in the case of diffusion and non-diffusion the grid cells near the particle surface take the following values: $a = \delta z/D = 1.5 \times 10^{-3}$, $b = \delta l/D = 1.5 \times 10^{-2}$ and $a = 3.3 \times 10^{-3}$, $b = 2 \times 10^{-2}$, respectively.

The under-relaxation factors for T and Y_i variables were set at 0.7 due to the strong coupling between the species and the energy conservation equations. The iterations were stopped when the maximal normalized residual for all equations was less than 10^{-7}. In order to reach the convergence 10^5, iterations were necessary.

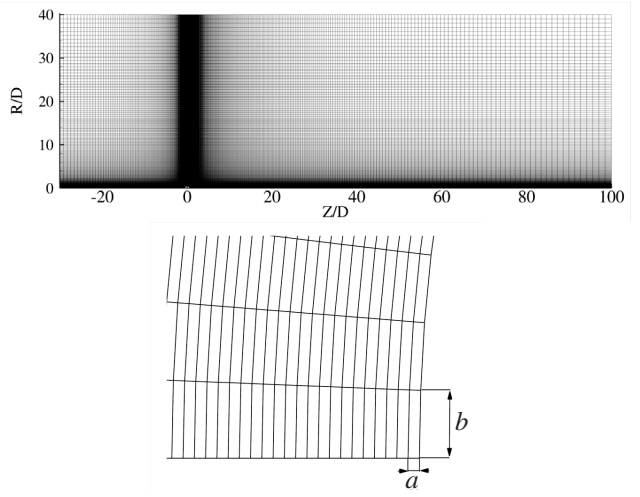

Figure 3

CFD-based model: computational grid used in simulations for $Re > 0$ and zoomed view near the particle surface. The grid cell near the particle surface takes the following values: $a = \delta z/D = 3.3 \times 10^{-3}$, $b = \delta l/D = 2 \times 10^{-2}$.

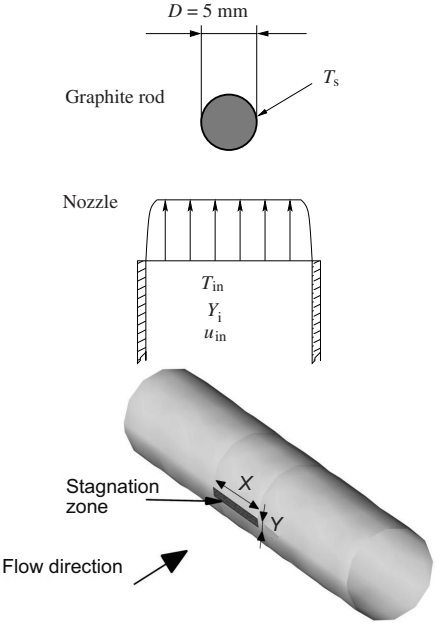

Figure 4

Schematic drawing of the experimental setup. Reproduced from [1].

The validation of the model and software against the analytic two-film model is reported in [25]. Next, we validate the software and the model we use against experiments by Makino *et al.* [1], where a graphite cylinder reacting with hot air was studied under laminar and turbulent flow conditions. The geometry and boundary conditions used in the validation are taken from the benchmark experiment, see Figure 4. In particular, to repeat the benchmark experiment

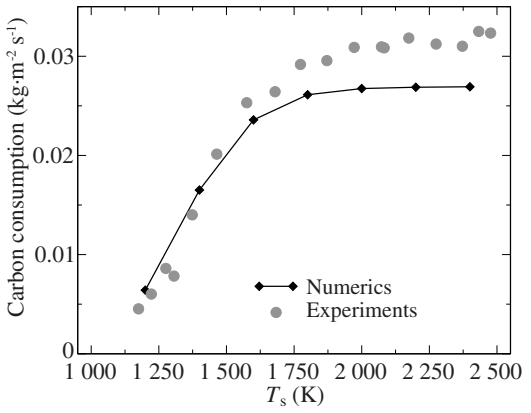

Figure 5

Carbon consumption rates in dependence on the rod surface temperature predicted numerically and experimentally [1] at $T_\infty = 320$ K and $a = 3\,300\ \mathrm{s}^{-1}$ corresponding to Re = [36:167] in dependence on the T_s. Different values of Re at constant a are explained by different values of the viscosity and density, which are temperature-dependent.

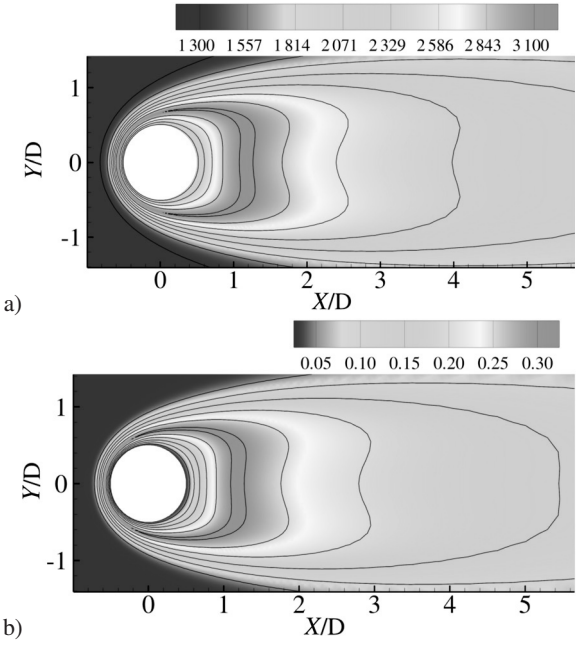

Figure 6

a) Contour plots of the temperature, b) CO_2 mass fraction, predicted numerically for laminar flow regime for $a = 3\,300\ \mathrm{s}^{-1}$. Here, $T_\infty = 320$ K and $T_s = 2\,000$ K.

by Makino *et al.* [1] numerically we consider a 2D computational domain shown in Figure 4. In particular, a 2D rod with a diameter $D = 5$ mm is placed (at coordinates $30D$ and $40D$) in the domain with a length of $130D$ and a height of $80D$. The ambient airflow temperature T_∞ is set to 320 K. The rod surface temperature T_s is varied between 1 200-2 500 K. In experiments by Makino *et al.* [1], the carbon combustion rate was measured in the forward-stagnation region, see Figure 4. The velocity gradient a_u (stretch rate, for details see the work [1]) in the forward stagnation point was set to $3\,300\ \mathrm{s}^{-1}$ corresponding to the range of the Reynolds number from 36 to 167 in dependence on T_s. The flow was laminar. It should be noted that the critical Reynolds numbers did not correspond to the well-known characteristic values for isothermal flows past a cylinder. Due to the high temperature gradients, the gas viscosity and density are changed significantly within the domain, which leads to a relaminisation effect.

An analysis of results applied to combustion rates reveals relatively good agreement between numerical and experimental data, see Figure 5. In particular, as expected, non-linear dependency can be detected between T_s and carbon consumption. The non-linearity characterizes two different combustion regimes. The first regime is a so-called kinetically controlled regime governed by kinetics. This regimes is defined by a rapid increase in carbon consumption rates with an increase in T_s. We note that for this regime very good agreement was achieved between the numerical results and experiments. The second regime is characterized by combustion rates approaching constant values. This regimes is called a diffusion-limited regime and is governed by convection-diffusion processes. For this regime, the disagreement between experimental and numerical data reaches about 10%. We explain this disagreement by the failure to take into account the porosity of the cylinder surface, which was reported in experiment [1]. In particular, our recent three-dimensional simulations of a porous char particle reacting in a stream of hot air showed that in a diffusion-limited regime CO_2 diffuses inside the pores and reacts with carbon leading to the increase in carbon consumption [51]. In conclusion, an illustration of this regime is shown in Figure 6, which depicts contour plots of the temperature and CO_2 mass fraction predicted numerically for a laminar flow regime at $a_u = 3\,300\ \mathrm{s}^{-1}$, $T_\infty = 320$ K and $T_s = 2\,000$ K. The so-called flame sheet can be detected, characterized by higher values of T and CO_2 around the rod. In particular, the CO oxidation in the boundary layer leads to the formation of a thin flame sheet where the CO_2 concentration and the temperature have their maxima. It should be noted that the basic features of the flame sheet can be described well using the two-film model, *e.g.* see the book [29].

5 RESULTS AND DISCUSSION

Below follows a description of the results validating the subgrid model developed for the partial oxidation of a char particle moving in a hot oxidizing environment. First, some

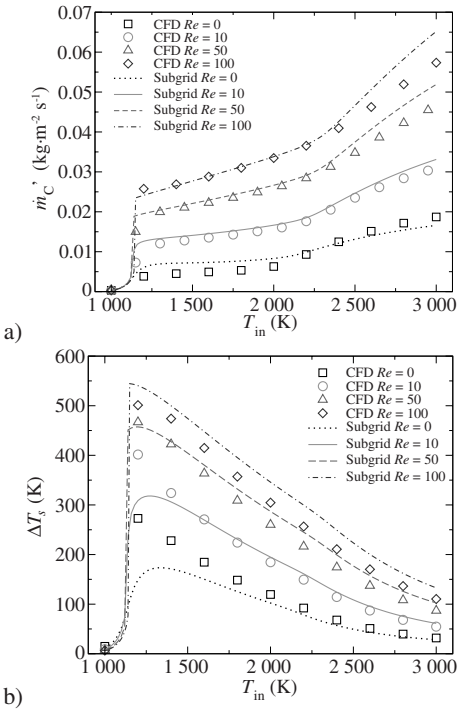

Figure 7

a) Carbon mass flux m'_C, b) temperature difference ΔT_s, at a carbon particle with a diameter of 2 mm and $Y_{O_2,\infty} = 0.233$ and $Y_{H_2O,\infty} = 0.001$. Here, $T_{in} = T_\infty$.

words should be said about the key parameters characterizing particle-gas interaction. In particular, the so-called specific gasification/combustion rate $\dot{m}'_C$ (see *Eq. 28*) and the difference between the ambient gas temperature and the particle surface temperature $\Delta T = (T_s - T_\infty)$ are the most important parameters governing the interaction between particles and gas, including the mass and the heat transfer.

The main operating variables which are basically used as input parameters in subgrid models are the particle Reynolds number (see *Eq. 1*), the ambient gas temperature $T_{in} = T_\infty$ and the ambient species mass fractions $Y_{i,\infty}$.

To proceed, first we discuss the results obtained for the first case corresponding to the so-called dry air atmosphere with 0.233 mass fraction of O_2 and 0.001 mass fraction of H_2O. In particular, to study the impact of the Reynolds number *Re* and the ambient temperature T_{in} on the particle oxidation behavior, several sets of simulations were performed. In every set, the Reynolds number was fixed and the ambient temperature T_{in} was varied between 1 000 K and 3 000 K in order to cover both kinetically-controlled and diffusion-controlled regimes. The results of simulations in the form of integral characteristics and spatial distributions obtained for the dry air case are shown in Figure 7 and Figures 8, 9, respectively. For instance, Figure 7 depicts the carbon mass flux $\dot{m}'_C$ and the temperature difference ΔT_s predicted numerically using a CFD-based model and a subgrid model. We note that the values $\dot{m}'_C$ and ΔT_s predicted using the CFD-based model correspond to the surface-averaged values. It can be seen that an increase in the particle velocity increases the particle mass loss rate. This statement is in good agreement with simulations carried out by Blake [22] and Higuera [23]. The $\dot{m}'_C$ values obtained using the subgrid model are very close to the data predicted utilizing CFD-based model. This close agreement was achieved due to parametric fitting of r_F, the values of which are given in Table 3 in the form r_F/r_S. It can be seen that an increase in the *Re* number increases r_F. This effect can be explained physically due to the enhancement of species transport near the particle surface as *Re* increases. Thus the role of homogeneous reactions near the surface increases.

TABLE 3

Radius ratio between the radius of the virtual sheet for homogeneous reactions used in a submodel and the radius of the particle, r_F/r_S

Case	$Re = 0$	$Re = 10$	$Re = 50$	$Re = 100$
Dry air	1.1	1.15	1.20	1.25
Reduced oxidation	1.02	1.03	1.04	1.05

An analysis of Figure 7b shows that, similarly to the very good agreement between the subgrid model predictions and the CFD-based model calculations regarding carbon consumption rates, the subgrid model produces a fairly accurate description of the values of ΔT_s calculated using the CFD-based model. Both models reveal that the temperature difference ΔT_s reaches its maxima in the interval between 1 200 K and 1 250 K. We found out that ΔT_s decreases as T_{in} increases, due to the flame detachment from the particle surface. To illustrate this effect, Figures 8 and 9 depict a zoomed view of the temperature contour plots calculated for the different ambient temperatures at constant *Re* equal to 10 and 100 for a particle size of $D = 2$ mm, respectively. It can be seen that in dependence on T_{in} three basic regimes can be generally identified. The definition of the regimes is based on the "visual" analysis of contour plots, *e.g.* distribution of the temperature and CO_2 around the particle. In particular, it can be seen that at the highest values of T_{in} ($T_{in} > 2\,000$ K) (see short comment (1) on the impact of *Re* on the regime change) the so-called envelope flame exists around a moving spherical particle, see Figures 8e and 9e. The flame shape covers the particle and is elongated in the direction of the flow. This well-known effect has been illustrated numerically and experimentally before by many authors. To link in with these effects, we refere to the works of Higuera [23] and Raghavan *et al.* [52], respectively.

A decrease in the ambient temperature leads to the transition from the envelope-flame regime to the so called surface-attached flame, see Figure 8b-d and Figure 9b-d. It can be

(1) It should be noted that the increase in *Re* leads to an increase in the temperature values where a change of regimes occurs.

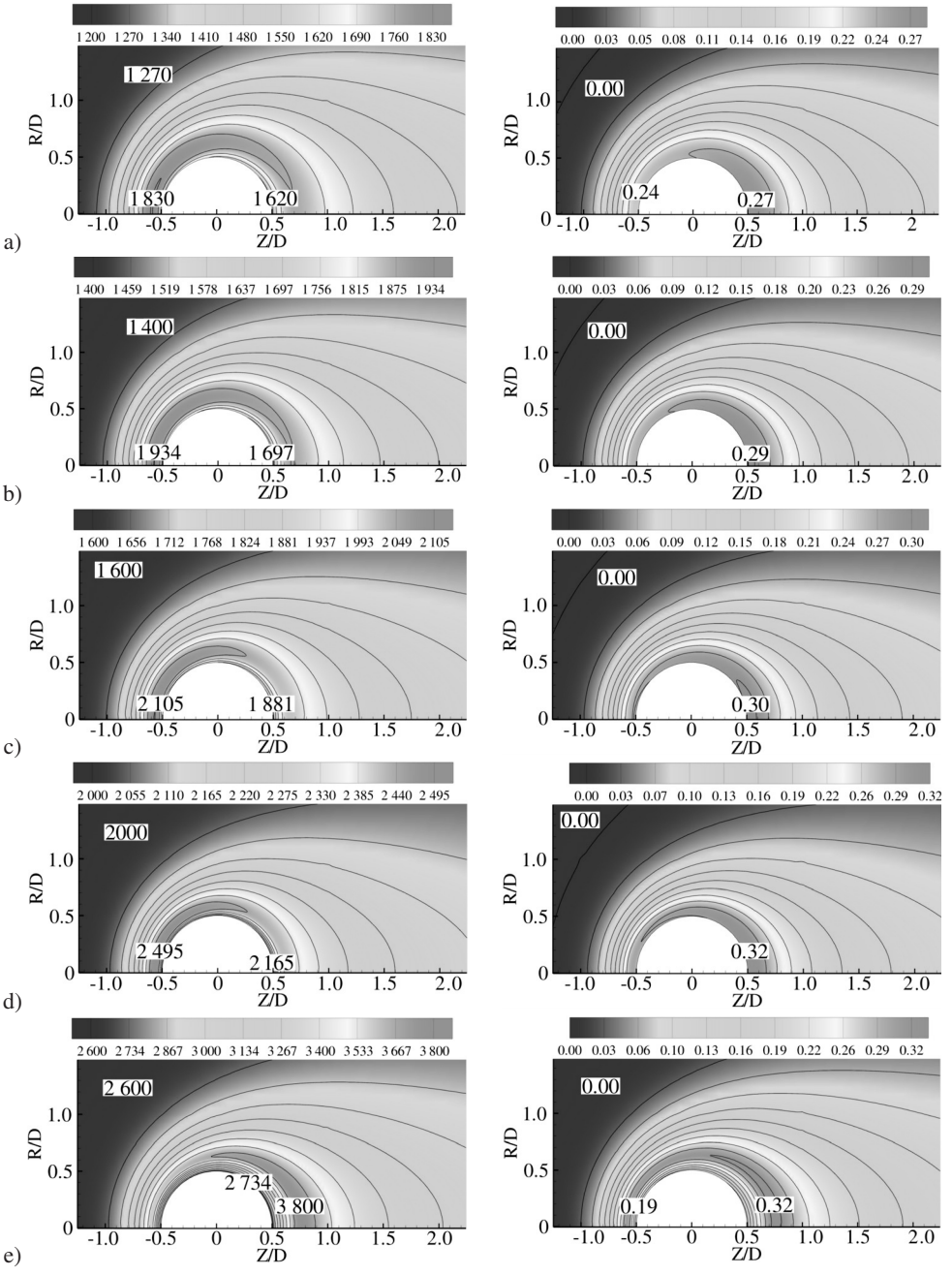

Figure 8

Contour plots of temperature (left) and CO_2 mass fraction (right) near to carbon particle with $D = 2$ mm, $Re = 10$ and a) $T_{in} = 1\,200$ K, b) $T_{in} = 1\,400$ K, c) $T_{in} = 1\,600$ K, d) $T_{in} = 2\,000$ K, e) $T_{in} = 2\,600$ K. The ambient mass fractions of O_2 and H_2O are 0.233 and 0.001, respectively.

seen that the CO_2 mass fraction is at a maximum at the particle surface. This effect is explained by the fact that CO oxidation occurs very close to the particle surface. At the same time, an analysis of a zoomed view of the temperature contour plots shows that the temperature does not reach its maximum value on the particle surface. Instead, a maximum T is located very close to the particle surface. This effect is attributed to the heterogeneous endothermic reaction 2 which leads to a decrease in T on the particle surface. It should be noted that in the front part of the particle surface the temperature is higher in comparison to the temperature in the rear part of the particle. This effect is related to the

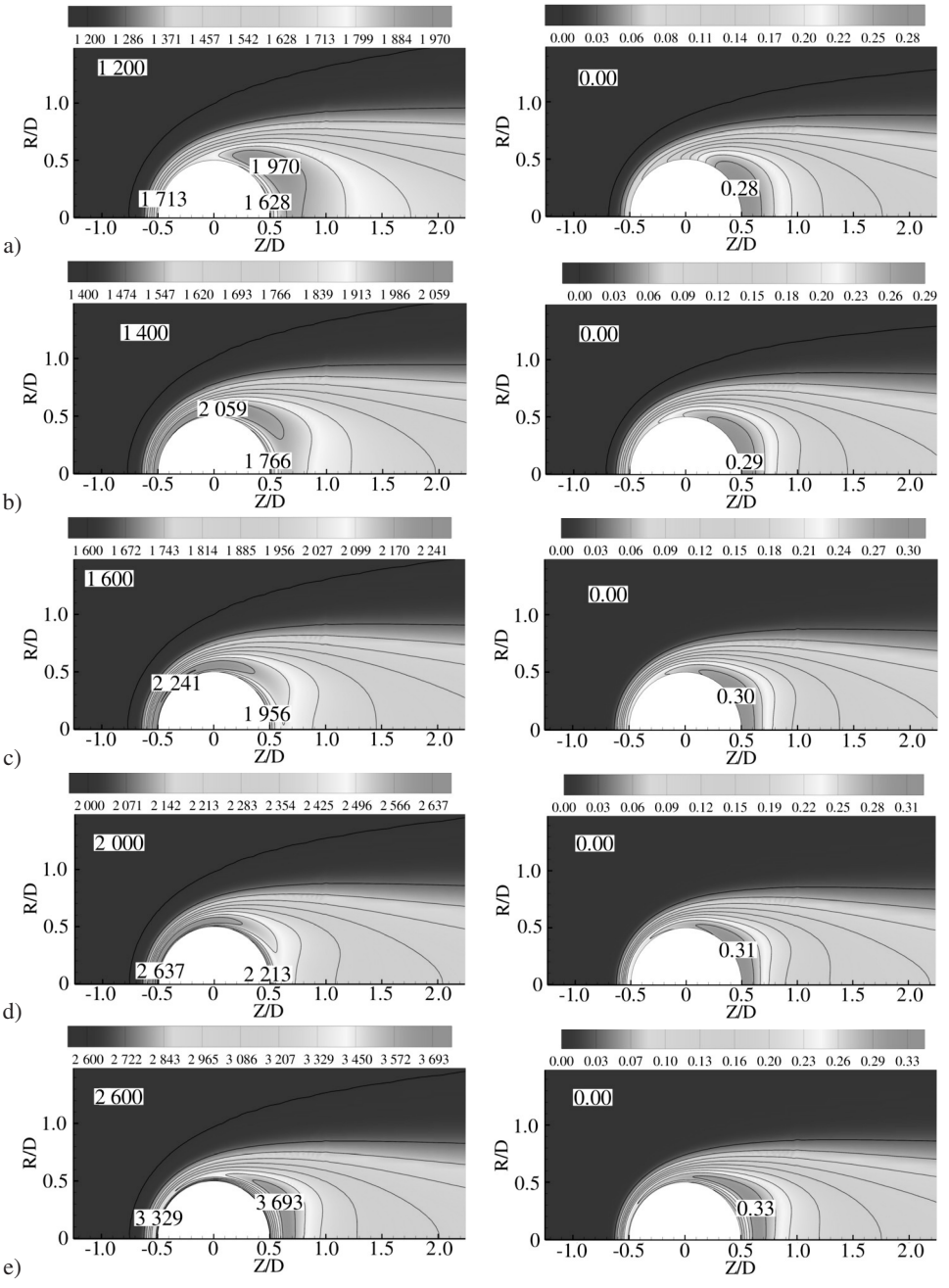

Figure 9

Contour plots of temperature (left) and CO_2 mass fraction (right) near to carbon particle with D = 2 mm, Re = 100 and a) T_{in} = 1 200 K, b) T_{in} = 1 400 K, c) T_{in} = 1 600 K, d) T_{in} = 2 000 K, e) T_{in} = 2 600 K. The ambient mass fractions of O_2 and H_2O are 0.233 and 0.001, respectively.

higher values of CO_2 mass fraction in the rear part of the particle. This disbalance in CO_2 is explained by the next regime.

A further decrease in the ambient temperature leads to the transition from the surface-attached flame regime to the so-called wake flame, see Figure 8a and Figure 9a. It can be seen that there is almost no CO oxidation in the front part of the particle surface. The flame, which can be detected at maximum CO_2 and T, is established only in the rear part of the particle (wake region). The increase in the particle Re number promotes the formation of the wake flame regime. This effect can be seen by comparing Figure 8a and

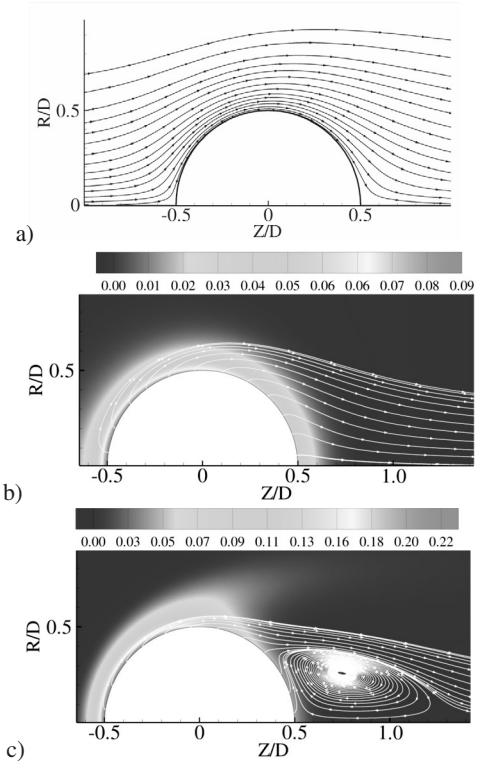

Figure 10

Streamlines and CO mass fraction near to carbon particle calculated for T_{in} = 1 600 K: a) Re = 10, isothermal case b) Re = 10 and c) Re = 100. The ambient mass fractions of O_2 and H_2O are 0.233 and 0.001, respectively. D = 2 mm.

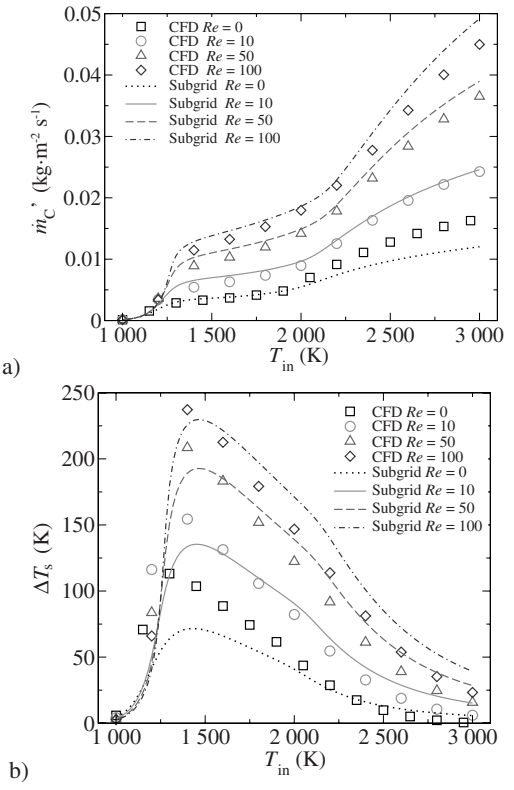

Figure 11

a) Carbon mass flux m'_C, b) temperature difference ΔT_s, for a carbon particle with a diameter of 2 mm and $Y_{O_2,\infty}$ = 0.11 and $Y_{H_2O,\infty}$ = 0.074.

Figure 9a, which show a zoomed view of Y_{CO_2} contour plots near the carbon particle calculated for Re = 10 and Re = 100 for the ambient temperature T_{in} = 1 200 K, respectively. Following findings by Raghavan *et al.* [52], the effect of the wake flame at high Re numbers is attributed to the flow separation in the recirculation zone, *e.g.* see Figure 10c. In particular, the extinction of the flame in the front part of the particle is attributed to the lower flow residence time in comparison to the reaction time. However, in the wake region, the recirculation flow increases the residence time for reactants. In the case of low particle Re numbers flows, on the other hand, where the recirculation does not exist, a similar wake flame regime can be observed, see Figure 10b. This effect is explained by the Stefan flow, which modifies the boundary layer thickness around the particle for low Re number flow regimes. In particular, Figure 10a shows that the isothermal flow past a sphere at Re = 10 does not have a recirculation zone. At the same time, in the case of chemically reacting particles the Stefan flow appears (see *Eq. 12*), changing the near-particle flow field in the downstream direction, see Figure 10b. Finally, this effect leads to the wake flame regime.

Next, we study the influence of the so-called reduced oxidation condition (which corresponds to the ambient gas composition with Y_{O_2} = 0.11 and Y_{H_2O} = 0.074) on the char particle behavior using the CFD-based model and subgrid models. The results of simulations using integral characteristics and spatial distributions are illustrated in Figure 11 and Figures 12, 13, respectively. In particular, Figure 11 depicts a comparison between the carbon mass flux $\dot{m}'_C$ and the temperature difference ΔT_s calculated using the CFD-based model and subgrid model. It can be seen that similarly to the previous dry air case the increase in the particle velocity increases the particle mass loss rate. However, due to the reduced oxygen concentration in the ambient gas the absolute values of $\dot{m}'_C$ are lower compared to similar values predicted for the dry air atmosphere, see Figure 7. An analysis of Figure 11b shows that the ignition interval, where the temperature difference ΔT_s reaches a maxima, is shifted to the higher temperatures between 1 200 K and 1 400 K (depending on Re), which is logical due to the reduced ambient concentration of O_2. Overall the increase in $\dot{m}'_C$ and ΔT_s in dependence on T_{in} is not as steep as the curves shown in Figure 7. Finally, it should be noted that the values

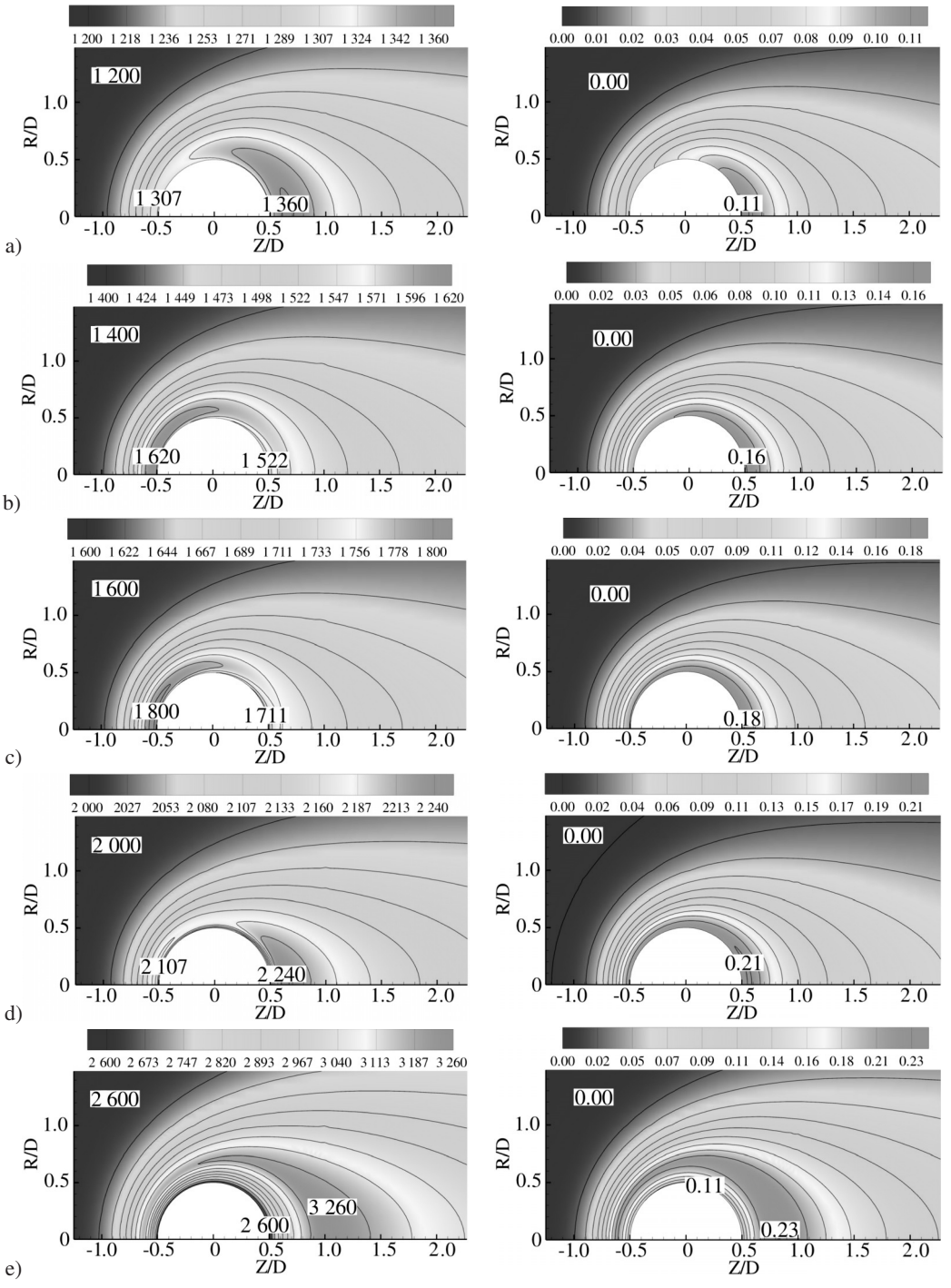

Figure 12

Contour plots of temperature (left) and CO_2 mass fraction (right) near to carbon particle with the D = 2 mm, Re = 10 and a) T_{in} = 1 200 K, b) T_{in} = 1 400 K, c) T_{in} = 1 600 K, d) T_{in} = 2 000 K, e) T_{in} = 2 600 K. The ambient mass fractions of O_2 and H_2O are 0.11 and 0.074, respectively.

for $\dot{m}'_C$ obtained using the subgrid model are very close to the data predicted utilizing a CFD-based model. This close agreement was achieved due to parametric fitting r_F, the values of which are given in Table 3 in the form r_F/r_S.

The analysis of the spatial distributions of the temperature and CO_2 mass fraction shown in Figures 12 and 13 depicts, similarly to the previous case, the so-called wake flame, surface-attached flame and flame envelope

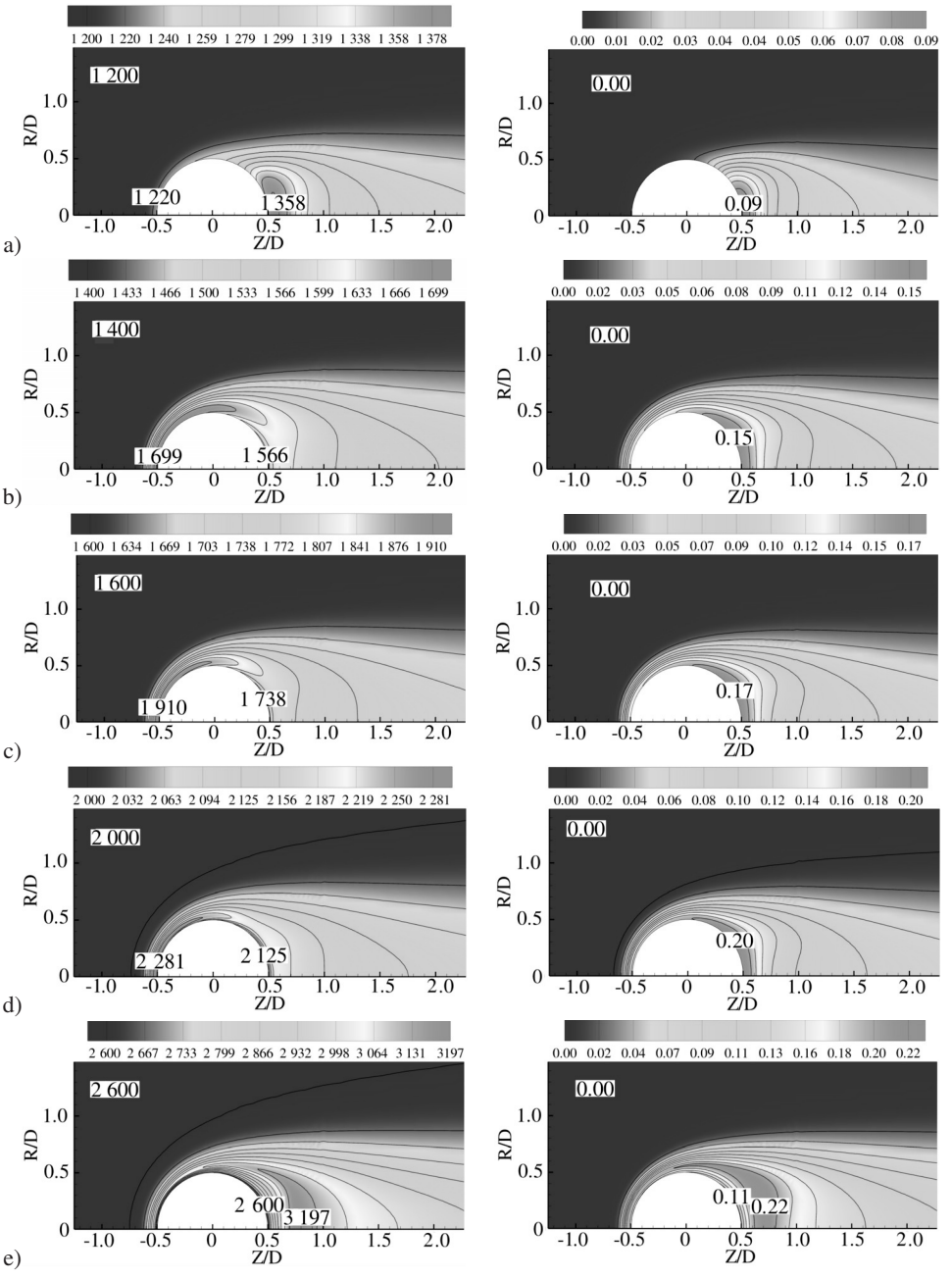

Figure 13

Contour plots of temperature (left) and CO_2 mass fraction (right) near to carbon particle with the $D = 2$ mm, $Re = 100$ and a) $T_{in} = 1\,200$ K, b) $T_{in} = 1\,400$ K, c) $T_{in} = 1\,600$ K, d) $T_{in} = 2\,000$ K, e) $T_{in} = 2\,600$ K. The ambient mass fractions of O_2 and H_2O are 0.11 and 0.074, respectively.

regimes in dependence on the ambient temperature and *Re* numbers.

To demonstrate the relevance of homogeneous reactions in the accurate prediction of the gasification/combustion rates for a single char particle moving in a hot environment, we introduce Figure 14, which repeats Figure 11 to some extent. However, the distinguishing feature of this figure is additional thin curves representing the results of the subgrid model, where the thickness of the virtual zone for homogeneous reactions was set to zero. It can be seen that failing to take into consideration homogeneous reactions in a subgrid model leads to the overestimation of

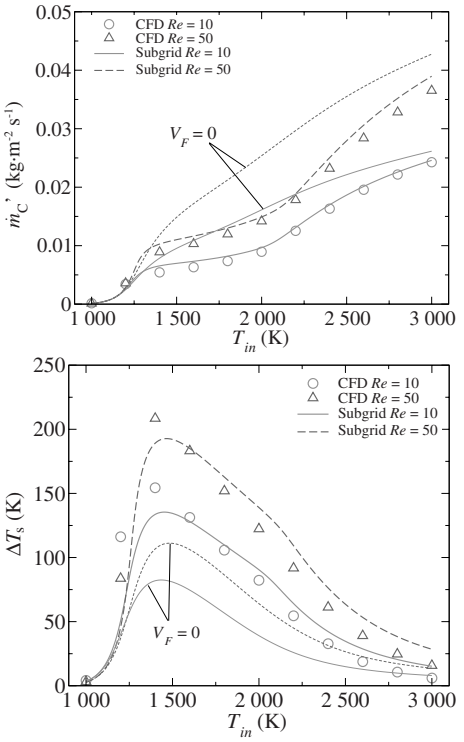

Figure 14

Carbon mass flux $\dot{m}'_C$ and temperature difference ΔT_s calculated for a char particle with a diameter of 2 mm at $Y_{O_2,\infty} = 0.11$ and $Y_{H_2O,\infty} = 0.074$. The icons represent results for the detailed numerical model: the thick lines show the results of the subgrid model with homogeneous reactions and the thin lines those without homogeneous reactions.

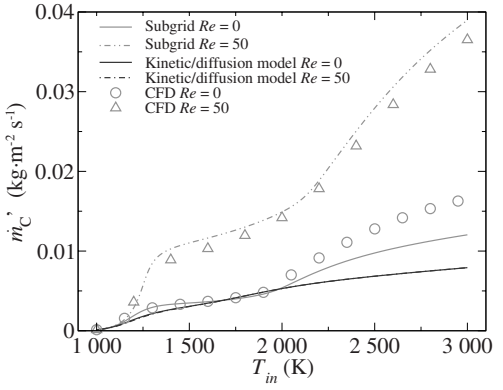

Figure 15

Carbon mass flux $\dot{m}'_C$ calculated using different models for a char particle with a diameter of 2 mm at $Y_{O_2,\infty} = 0.11$ and $Y_{H_2O,\infty} = 0.074$.

carbon consumption rates and underestimation of the particle temperature. This is quite an interesting result considering that mainstream kinetic-diffusion-based models, *e.g.* see the works [13, 14], do not take this effect into account. To compare the performances of the subgrid model, we have developed with a kinetic-diffusion-based model, in Figure 15 we plot the carbon mass flux calculated for a particle with a diameter of 2 mm using different models. In particular, the kinetic-diffusion-based model is introduced in Appendix B. As expected, the kinetic-diffusion-based model shows poor performance for large *Re* numbers in comparison to the submodel developed in this work. This is explained by the fact that it does not take into account the convection effects or consider the interfacial species mass fraction when calculating the carbon consumption rate.

CONCLUSIONS

In this work, we developed and validated a sub-model for the partial oxidation of a spherical char particle with a diameter of 2 mm moving in an air/steam atmosphere. The submodel includes six gaseous chemical species (O_2, CO_2, CO, H_2O, H_2, N_2). Three semi-global heterogeneous reactions are employed, along with two semi-global homogeneous reactions, namely carbon monoxide oxidation and the water-gas shift reaction. The subgrid model takes into account the influence of homogeneous reactions on integral characteristics such as carbon gasification/combustion rates and the temperature difference between the particle surface temperature and the ambient temperature. Failing to take into consideration homogeneous reactions leads to the overestimation of carbon consumption rates and the underestimation of the particle temperature. The submodel was validated by comparing its results with a comprehensive CFD-based model, which was verified against experimental data published in the literature. The submodel allows insights into the details of the moving char particle's behaviour without performing sophisticated and time-consuming CFD-based simulations. Additionally, this model allows us to study the relative influence of various design and operating parameters.

ACKNOWLEDGMENTS

The authors appreciate the financial support of the Government of the Free State of Saxony and the Federal Ministry of Education and Research of the Federal Republic of Germany as a part of the Center of Innovation Competence Virtuhcon. Finally, we would like to thank an anonymous reviewer for providing a number of constructive comments.

REFERENCES

1 Makino A., Namikiri T., Kimura K. (2003) Combustion rates of graphite rods in the forward stagnation field with high-temperature airflow, *Combust. Flame* **132**, 743-753.

2 Higman C., Van der Burgt M. (2003) *Gasification*, Elsevier Science, USA.

3 Buhre B.J.P., Elliott L.K., Sheng C.D., Gupta R.P., Wall T.F. (2005) Oxy-fuel combustion technology for coal-fired power generation, *Progr. Energ. Combust. Sci.* **31**, 283-307.

4 Wall T., Liu Y., Spero C., Elliott L., Khare S., Rathnam R., Zeenathal F., Moghtaderi B., Buhre B., Sheng C., Gupta R., Yamada T., Makino K., Yu J. (2009) An overview on oxyfuel coal combustion – State of the art research and technology development, *Chem. Eng. Res. Des.* **87**, 1003-1016.

5 Hanjalic K., Sijercic M. (1994) Application of computer simulation in a design study of a new concept of pulverized coal gasification. Part I. Rationale of the concept and model of hydrodynamics and heat transfer in the reactor, *Combust. Sci. Technol.* **97**, 331-350.

6 Sijercic M., Hanjalic K. (1994) Application of computer simulation in a design study of a new concept of pulverized coal gasification. Part II. Model of coal reactions and discussion of results, *Combust. Sci. Technol.* **97**, 351-375.

7 Chen C., Horio M., Kojima T. (2000) Numerical simulation of entrained flow coal gasifiers. Part I: Modeling of coal gasification in an entrained flow gasifier, *Chem. Eng. Sci.* **55**, 3861-3874.

8 Silaen A., Wang. T. (2010) Effect of turbulence and devolatilization models on coal gasification simulation in an entrained-flow gasifier, *Int. J. Heat Mass Trans.* **53**, 2074-2091.

9 Chen C.J., Hung C.I., Chen W.H. (2012) Numerical investigation on performance of coal gasification under various injection patterns in an entrained flow gasifier, *Appl. Energy* **100**, 218-228. http://dx.doi.org/10.1016/j.apenergy.2012.05.013.

10 Edge P., Gharebaghi M., Irons R., Porter R., Porter R.T.J., Pourkashanian M., Smith D., Stephenson P., Williams A. (2011) Combustion modelling opportunities and challenges for oxy-coal carbon capture technology, *Chem. Eng. Res. Des.* **89**, 1470-1493.

11 Armstrong L.M., Gu S., Luo K. (2010) CFD modelling of the gasification of coal particles in fluidized beds, *14th Int. Heat Transfer Conference*, by ASME, Washington, D.C., USA 8-13 Aug.

12 Oevermann M., Gerber S., Behrendt F. (2009) Euler-Lagrange/DEM simulation of wood gasification in a bubbling fluidized bed reactor, *Particuology* **7**, 307-316.

13 Baum M.M., Street P. (1971) Predicting the combustion behaviour of coal particles, *Combust. Sci. Technol.* **3**, 231-243.

14 Smith I.W. (1971) Kinetics of combustion of size-graded pulverized fuels in the temperature range 1200-2270 K, *Combust. Flame* **17**, 303-314.

15 Tu C.M., Davis H., Hottel H.C. (1934) Combustion rate of carbon. Combustion of spheres in flowing gas stream, *Ind. Eng. Chem.* **26**, 749-757.

16 Parker A., Hottel H.C. (1936) Combustion rate of carbon. Study of gas-film structure by microsampling, *Ind. Eng. Chem.* **28**, 1334-1341.

17 Kumar M., Ghoniem A.F. (2012) Multiphysics Simulations of Entrained Flow Gasification. Part II: Constructing and Validating the Overall Model, *Energy Fuels* **26**, 464-479.

18 Hayhurst A.N. (2000) The mass transfer coefficient for oxygen reacting with a carbon particle in a fluidized or packed bed, *Combust. Flame* **121**, 679-688.

19 Williams A., Pourkashanian M., Jones J.M. (2001) Combustion of pulverised coal and biomass, *Progr. Energ. Combust. Sci.* **27**, 587-610.

20 Maloneya D.J., Monazam E.R., Casleton K.H., Shaddix C.R. (2005) Evaluation of char combustion models: measurement and analysis of variability in char particle size and density, *Proc. Combust. Inst.* **30**, 2197-2204.

21 Molina A., Shaddix C.R. (2007) Ignition and devolatilization of pulverized bituminous coal particles during oxygen/carbon dioxide coal combustion, *Proc. Combust. Inst.* **31**, 1905-1912.

22 Blake T.R. (2002) Low Reynolds number combustion of a spherical carbon particle, *Combust. Flame* **129**, 87-111.

23 Higuera F.J. (2008) Combustion of a coal particle in a stream of dry gas, *Combust. Flame* **152**, 230-244.

24 Kestel M., Nikrityuk P.A., Meyer B. (2010) Numerical study of partial oxidation of a single coal particle in a stream of air, *Proceeding of 14th Int. Heat Transfer Conference*, by ASME, Washington D.C., USA, 8-13 Aug., CD: ISBN 978-0-7918-3879-2.

25 Kestel M., Nikrityuk P.A., Hennig O., Hasse C. (2012) Numerical study of the partial oxidation of a coal particle in steam and dry air atmospheres, *IMA J. Appl. Math.* **77**, 32-46.

26 Lee J.C., Yetter R.A., Dryer F.L. (1995) Transient numerical modeling of carbon particle ignition and oxidation, *Combust. Flame.* **101**, 387-398.

27 Nikrityuk P.A., Gräbner M., Kestel M., Meyer B., Numerical study of the influence of heterogeneous kinetics on the carbon consumption by oxidation of a single coal particle, *Fuel*, under 2nd review, in press.

28 Smith D.F., Gudmundsen A. (1931) Mechanism of combustion of individual particles of solid fuels, *Ind. Eng. Chem.* **23**, 277-285.

29 Turns S.R. (2000) *An Introduction to Combustion*, 2nd ed., McGraw-Hill, Boston, USA.

30 Dryer F.L., Glassman I. (1973) High temperature oxidation of CO and CH_4, *Proc. Combust. Inst.* **14**, 987-1003.

31 Wu Y., Smith Ph.J., Zhang J., Thornock J.N., Yue. G. (2010) Effects of turbulent mixing and controlling mechanisms in an entrained flow coal gasifier, *Energy Fuels* **24**, 1170-1175.

32 Chelliah H.K. (1995) Numerical modelling of graphite combustion using elementary, reduced and semi-global heterogeneous reaction mechanisms, in *Modelling in Combustion Science*, Buckmaster J., Takeno T. (eds), Springer, Berlin, pp. 130-147.

33 Chelliah H.K., Makino A., Kato I., Arki N., Law CK. (1996) Modeling of graphite oxidation in a stagnation-point flow field using detailed homogeneous and semiglobal heterogeneous mechanisms with comparisons to experiments, *Combust. Flame.* **104**, 469-480.

34 Sundaresan S., Amundson N.R. (1980) Diffusion and reaction in a stagnant boundary layer about a carbon particle. 5. Pseudo-steady-state structure and parameter sensitivity, *Ind. Eng. Chem. Fundam.* **19**, 344-351.

35 Tomboulides A.G., Lee J.C.Y., Orszag S.A. (1997) Numerical simulation of low Mach number reactive flows, *J. Sci. Comput.* **12**, 139-167.

36 Bathia S.K., Perlmutter D.D. (1980) A Random pore model for fluid-solid reactions: I. Isothermal, kinetic control, *AIChE J.* **26**, 379-386.

37 Everson R., Neomagus H., Kaitano R. (2005) The modeling of the combustion of high-ash coal-char particles suitable for pressurised fluidized bed combustion: shrinking reacted core model, *Fuel* **84**, 1136-1143.

38 Ahmed I.I., Gupta A.K. (2011) Particle size, porosity and temperature effects on char conversion, *Appl. Energy* **88**, 4667-4677.

39 Wittig K., Golia A., Nikrityuk P.A. (2012) 3D Numerical study of the influence of particle porosity on the heat and fluid flow, *Prog. Comput. Fluid Dynam.* **12**, 207-219.

40 Kee R.J., Coltrin M.E., Glarborg P. (2003) *Chemically Reacting Flow*, Wiley-Interscience, New York.

41 Caram H.S., Amundson N.R. (1977) Diffusion and reaction in a stagnant boundary layer about a carbon particle, *Ind. Eng. Chem. Fundam.* **16**, 171-181.

42 Libby P.A., Blake Th.R. (1981) Burning carbon particles in the presence of water vapor, *Combust. Flame* **41**, 123-147.

43 Jones W.P., Lindstedt R.P. (1988) Global reaction schemes for hydrocarbon combustion, *Combust. Flame* **73**, 233-249.

44 McBride B.J., Gordon S., Reno M.A. (1993) Coefficients for calculating thermodynamic and transport properties of individual species, *NASA Technical Memorandum* **4513**.

45 ANSYS-FLUENT^{TM} V 13.0 – Commercially available CFD software package based on the Finite Volume method. Southpointe, 75 Technology Drive, Canonsburg, PA 15317, USA, www.ansys.com (2011).

46 de Souza-Santos M.L. (2010) *Solid Fuels Combustion and Gasification*, 2nd ed., CRC Press, 6000 Broken Sound Parkway NW, Suite 300.

47 Ranz W.E., Marshall W.R. (1952) Evaporation of drops, *Chem Eng. Proc.* **48**, 173-180.

48 Schmidt R., Nikrityuk P.A. (2012) Numerical simulation of the transient temperature distribution inside moving particles, *Can. J. Chem. Eng.* **90**, 246-262.

49 Patankar S.V. (1980) *Numerical Heat Transfer and Fluid Flow*, Hemisphere Publishing, Corp., Washington, DC.

50 Leonard B.P. (1979) A stable and accurate convection modeling procedure based on quadratic up-stream interpolation, *Comp. Meth. Appl. Mech. Eng.* **19**, 59-68.

51 Richter A., Nikrityuk P. (2012) Three-dimensional calculation of a chemically reacting coal-particle agglomerate moving in hot air. *9th European Conference on Coal Research and its Applications: ECCRIA 9*, University of Nottingham, UK, 10-12 Sept.

52 Raghavan V., Babu V., Sundararajan T., Natarajan R. (2005) Flame shapes and burning rates of spherical fuel particles in a mixed convective environment, *Int. J. Heat Mass Trans.* **48**, 5354-5370.

Final manuscript received in September 2012
Published online in April 2013

APPENDIX A

Next, we present the basic equations of the subgrid model, see Equations (19) and (23), written out in detail.

The thermal energy balance for a char particle takes the form:

$$\begin{aligned} m_p\, c_p\, \frac{dT_s}{dt} &= A_p\, \left(\alpha\,(T_\infty - T_s) + \varepsilon_S\, \sigma \left(T_\infty^4 - T_s^4\right)\right) \\ &\quad - A_P\, \rho_s\, M_{\mathrm{C}}\, Q_R^S - V_F\, M_{\mathrm{CO}}\, \left(Q_R^{V1} + Q_R^{V2}\right) \end{aligned} \tag{A.1}$$

$$\begin{aligned} Q_R^S &= \frac{Y_{\mathrm{O_2},S}}{M_{\mathrm{O_2}}}\, k_{R1}\, h_{R1}^0 + \frac{Y_{\mathrm{CO_2,S}}}{M_{\mathrm{CO_2}}}\, k_{R2}\, h_{R2}^0 + \frac{Y_{\mathrm{H_2O,S}}}{M_{\mathrm{H_2O}}}\, k_{R3}\, h_{R3}^0 \\ Q_R^{V1} &= \rho_S^{1.75}\, \frac{Y_{\mathrm{CO},S}}{M_{\mathrm{CO}}}\, \cdot \left(\frac{Y_{\mathrm{O_2},S}}{M_{\mathrm{O_2}}}\right)^{0.25}\, \cdot \left(\frac{Y_{\mathrm{H_2O},S}}{M_{\mathrm{H_2O}}}\right)^{0.5}\, k_{R4}\, h_{R4}^0 \\ Q_R^{V2} &= \rho_S^2\, \frac{Y_{\mathrm{H_2O},S}}{M_{\mathrm{H_2O}}}\, \frac{Y_{\mathrm{CO},S}}{M_{\mathrm{CO}}} k_{R5} h_{R5}^0 + \rho_S^2\, \frac{Y_{\mathrm{H_2},S}}{M_{\mathrm{H_2}}}\, \frac{Y_{\mathrm{CO_2},S}}{M_{\mathrm{CO_2}}} k_{R6} h_{R6}^0 \end{aligned} \tag{A.2}$$

Balance equations for chemical species :

$Y_{\mathrm{O_2}}$:

$$\begin{aligned} &\frac{\beta\, \rho_S}{M_{\mathrm{O_2}}}\, \left(Y_{\mathrm{O_2},\infty} - Y_{\mathrm{O_2},S}\right) = \rho_S\, \frac{Y_{\mathrm{O_2},S}}{M_{\mathrm{O_2}}}\, k_{R1} \\ &+ \frac{V_F}{A_P} \left(0.5\, \rho_s^{1.75}\, \frac{Y_{\mathrm{CO},S}}{M_{\mathrm{CO}}}\, \left(\frac{Y_{\mathrm{O_2},S}}{M_{\mathrm{O_2}}}\right)^{0.25}\, \left(\frac{Y_{\mathrm{H_2O},S}}{M_{\mathrm{H_2O}}}\right)^{0.5}\, k_{R4}\right) \end{aligned} \tag{A.3}$$

$Y_{\mathrm{CO_2}}$:

$$\begin{aligned} &\frac{\beta\, \rho_S}{M_{\mathrm{CO_2}}}\, \left(Y_{\mathrm{CO_2},\infty} - Y_{\mathrm{CO_2},S}\right) = \rho_S\, \frac{Y_{\mathrm{CO_2},S}}{M_{\mathrm{CO_2}}}\, k_{R2} \\ &- \frac{V_F}{A_P} \left(\rho_s^{1.75}\, \frac{Y_{\mathrm{CO},S}}{M_{\mathrm{CO}}}\, \left(\frac{Y_{\mathrm{O_2},S}}{M_{\mathrm{O_2}}}\right)^{0.25}\, \left(\frac{Y_{\mathrm{H_2O},S}}{M_{\mathrm{H_2O}}}\right)^{0.5}\, k_{R4}\right) \\ &- \frac{V_F}{A_P} \left(\rho_S^2\, \frac{Y_{\mathrm{H_2O},S}}{M_{\mathrm{H_2O}}}\, \frac{Y_{\mathrm{CO},S}}{M_{\mathrm{CO}}} k_{R5}\right) + \frac{V_F}{A_P} \left(\rho_S^2\, \frac{Y_{\mathrm{H_2},S}}{M_{\mathrm{H_2}}}\, \frac{Y_{\mathrm{CO_2},S}}{M_{\mathrm{CO_2}}} k_{R6}\right) \end{aligned} \tag{A.4}$$

$Y_{\mathrm{H_2O}}$:

$$\begin{aligned} &\frac{\beta\, \rho_S}{M_{\mathrm{H_2O}}}\, \left(Y_{\mathrm{H_2O},\infty} - Y_{\mathrm{H_2O},S}\right) = \rho_S\, \frac{Y_{\mathrm{H_2O},S}}{M_{\mathrm{H_2O}}}\, k_{R3} \\ &+ \frac{V_F}{A_P} \left(\rho_S^2\, \frac{Y_{\mathrm{H_2O},S}}{M_{\mathrm{H_2O}}}\, \frac{Y_{\mathrm{CO},S}}{M_{\mathrm{CO}}}\, k_{R5}\right) \\ &- \frac{V_F}{A_P} \left(\rho_S^2\, \frac{Y_{\mathrm{H_2},S}}{M_{\mathrm{H_2}}}\, \frac{Y_{\mathrm{CO_2},S}}{M_{\mathrm{CO_2}}}\, k_{R6}\right) \end{aligned} \tag{A.5}$$

$Y_{\mathrm{H_2}}$:

$$\begin{aligned} &\frac{\beta\, \rho_S}{M_{\mathrm{H_2}}}\, \left(Y_{\mathrm{H_2},\infty} - Y_{\mathrm{H_2},S}\right) = -\rho_S\, \frac{Y_{\mathrm{H_2O},S}}{M_{\mathrm{H_2O}}}\, k_{R3} \\ &- \frac{V_F}{A_P} \left(\rho_S^2\, \frac{Y_{\mathrm{H_2O},S}}{M_{\mathrm{H_2O}}}\, \frac{Y_{\mathrm{CO},S}}{M_{\mathrm{CO}}}\, k_{R5}\right) \\ &+ \frac{V_F}{A_P} \left(\rho_S^2\, \frac{Y_{\mathrm{H_2},S}}{M_{\mathrm{H_2}}}\, \frac{Y_{\mathrm{CO_2},S}}{M_{\mathrm{CO_2}}}\, k_{R6}\right) \end{aligned} \tag{A.6}$$

Y_{CO}:

$$\begin{aligned}
&\frac{\beta\,\rho_S}{M_{CO}}\,(Y_{CO,\infty}-Y_{CO,S}) = -2\,\rho_S\,\frac{Y_{O_2,S}}{M_{O_2}}\,k_{R1}\\
&-2\,\rho_S\,\frac{Y_{CO_2,S}}{M_{CO_2}}\,k_{R2} - \rho_S\,\frac{Y_{H_2O,S}}{M_{H_2O}}\,k_{R3}\\
&+\frac{V_F}{A_P}\left(\rho_s^{1.75}\,\frac{Y_{CO,S}}{M_{CO}}\left(\frac{Y_{O_2,S}}{M_{O_2}}\right)^{0.25}\left(\frac{Y_{H_2O,S}}{M_{H_2O}}\right)^{0.5}\,k_{R4}\right)\\
&+\frac{V_F}{A_P}\left(\rho_S^2\,\frac{Y_{H_2O,S}}{M_{H_2O}}\,\frac{Y_{CO,S}}{M_{CO}}\,k_{R5}\right)\\
&-\frac{V_F}{A_P}\left(\rho_S^2\,\frac{Y_{H_2,S}}{M_{H_2}}\,\frac{Y_{CO_2,S}}{M_{CO_2}}\,k_{R6}\right)
\end{aligned} \tag{A.7}$$

This system of equations representing the subgrid model has to be solved iteratively for each time step. In this work, we used the bisectional method to solve this system of equations.

APPENDIX B

The kinetic/diffusion model is widely used in commercial CFD codes to describe the combustion of char particles. The kinetic/diffusion-limited model considers that the surface reaction is controlled by both kinetics and diffusion. The diffusion rate coefficient D_0 used in the model is gained from the ratio of diffusion coefficient to particle diameter:

$$D_{Y0} = \frac{D_Y}{2\,r_p} \tag{B.1}$$

The diffusion coefficient is calculated by assuming the Lewis number to be about unity:

$$D_Y = \frac{\lambda}{c_p\,\rho} \tag{B.2}$$

The kinetic rate coefficient is calculated from the Arrhenius expression as the following:

$$k = A_r\,T^{n_r}\exp(-E_A/(R\,T_s)) \tag{B.3}$$

The carbon mass balance is derived from a harmonic weighting of the diffusion rate coefficient and kinetic rate coefficient. Therefore, the carbon mass balance in the case of a single oxidizing species is:

$$\dot{m}_C = A_P\,\rho\frac{M_{ox}}{M_C}\,Y_{ox}\frac{D_{Y0}\,k}{D_{Y0}+k} \tag{B.4}$$

To adopt the kinetic/diffusion model for our problem, more than one heterogeneous reaction has to be taken into account. At first, there are two oxidizing ambient gas species which are used in the carbon mass balance for multi-species reactions:

$$\dot{m}_C = A_P\,\rho\left(\frac{M_{O_2}}{M_C}\,Y_{O_2}\frac{D_{Y0}\,2\,k_{R1}}{D_{Y0}+k_{R1}} + \frac{M_{H_2O}}{M_C}\,Y_{H_2O}\frac{D_{Y0}\,k_{R3}}{D_{Y0}+k_{R3}}\right) \tag{B.5}$$

The heat balance is established in a similar way to the previous subgrid model (see *Eq. A.1*).